Removal of Toxic Dyes from Industrial Waste Water using Chitosan Grafted Itaconic Acid Nanocomposites

M. Swathi[1], Pratik Roy[2], M. V. Deepthi[2], R. R. N. Sailaja[2,*]

[1]Agricultural Engineering College & Research Institute, Tamil Nadu Agricultural University, Coimbatore 641003, India
[2]The Energy and Resources Institute, Southern Regional Centre, Bangalore 560071, India

***Corresponding author: E-mail: sailaja.bhattacharya@gmail.com; sailajab@teri.res.in; Fax: (080) 25356589**

DOI: 10.5185/amlett.2021.061639

In this study chitosan (CTS) has been grafted with itaconic acid (IA) by following microwave assisted grafting method. Three different types of nanomaterials namely nanoclay, cloisite 30B and multiwalled carbon nanotubes (MWCNT) have also been incorporated during the grafting reaction. The synthesized nanocomposites were used for the removal of napthol green, reactive black and congo red dyes from aqueous solutions. Results showed enhanced dye adsorption capacity after addition of nanomaterials. The adsorption isotherm fitted well with Langmuir model. It was observed that CTS grafted IA composite with cloisite 30B exhibited highest napthol green adsorption rate compared to others. CTS grafted IA composite with MWCNT showed better congo red and reactive black adsorption rate as compared to CTS nanocomposite modified with nanoclay and cloisite 30B. The swelling kinetics in acidic, basic and neutral medium was found to follow pseudo second order kinetic model. Fourier transform infrared spectroscopy (FTIR) analysis showed successful grafting of IA on CTS. X-ray diffraction (XRD) and morphological characteristics suggested enhanced dispersion of nanomaterials in CTS matrix.

Introduction

The usage of a wide number of synthetic dyes in various applications has become a major environmental concern as it pollutes water bodies [**1**]. There are significant amount of harmful dyes present in the wastewater discharged from dyeing, textile, leather, paper, rubber, plastics, pharmaceuticals and food industry. This in turn contaminates water bodies which lead to harmful effects [**2**]. Hence, there is an essential requirement to remove these dyes before being discharged into various water bodies. With the progress in the science and technology, advanced methods for toxic dye removal have been tested successfully. One such technique for removal of dyes is through adsorption method, as it is highly efficient and hassle free. The development of hydrogels based on bio-polymeric materials for adsorption purposes is gaining importance as they are eco-friendly, inexpensive and cost-effective [**3**]. Ease of operation and high efficiency has thus prompted the use of natural biopolymers such as chitosan and chitin.

Sanghi *et. al.* reviewed and discussed various possible inexpensive adsorbents from natural resources for the removal of dyes from waste water [**4**]. Szymczyk *et. al.* compared the efficiency of chitin and chitosan for the removal of reactive black dye. Chitosan (CTS) has higher adsorption capacity than chitin as the former has higher number of amine groups [**5**]. Ignat *et. al.* found that dye structure and kinetic parameters influence the adsorption capacity of chitosan. Thus, CTS showed higher adsorption to reactive red dye as compared to brown 95 [**6**]. Vakili *et. al.* reviewed the use of CTS and its derivatives for removal of dyes from water. It has been discussed that modification of CTS (Via grafting, crosslinking etc.) led to enhanced adsorption efficiency than raw CTS [**7**]. Several researchers found that modified CTS showed higher adsorption efficiency than raw CTS for the removal of both cationic and anionic dyes. The increased efficacy has been attributed to the availability of excess carboxyl groups due to modification [**8-14**]. Similar observation on the enhancement of carboxyl group on modified CTS has been reported by Yu *et. al.* [**15**]. A blend of CTS and spirulina were cast into films for the adsorption of methylene blue, tartrazine yellow and reactive black. It was found that the adsorption capacity was enhanced for tartrazine yellow and reactive black with increase in CTS content while variation in spirulina content influenced methylene blue adsorption [**16**].

The use of nanosized materials such as montmorillonite (MMT) has been found to enhance adsorption efficiencies. Hence, CTS/MMT nano-composites have been found to have high adsorption capacity for the congo red dye. The adsorption was found to follow Langmuir isotherm and pseudo-second order kinetics [**17**]. Kaemkit *et. al.* studied the effects of water soluble CTS/ MMT composite for removal of basic blue and basic yellow dyes. It was interesting to note that percentage adsorption of dyes using nanocomposite was higher than using chitosan and MMT separately [**18**]. This suggests that using CTS and nanomaterial together exhibit positive synergism rather than using them separately. Nanobiocomposite comprised of CTS and cloisite 30B was found to show promising potential for reactive blue and reactive red. The adsorption parameters have been optimized while thermodynamic evaluation indicated spontaneous reaction [**19**]. Wang *et. al.* studied the effect of (CTS) /MMT on congo red dye removal. The adsorption capacity was found to depend on MMT loading, pH value and temperature [**20**]. Studies on removal of dyes using CTS grafted itaconic acid (IA) are very few. CTS was modified and then grafted with amine functionalized MWCNT. The modified CTS was found to remove both Pb^{2+} ions and 99% of the phthalocyanine dye. It was found that MWCNT have higher specific surface area which contributed to the high efficiency of dye removal [**21**]. Similar observations have been made for the removal of brilliant green dye [**22**]. It was suggested that boundary layer and intra-particle diffusion influenced dye removal efficiency.

In this study, IA has been grafted to CTS with the inclusion of three types of nanosized particles. The effect of these nanocomposite adsorbents on dye removal has been studied and compared. The removal efficiency of these three types of nanocomposites has been separately studied to examine the effect of the type of nanomaterial on the adsorption of dyes. Such studies could not be cited from literature.

Experimental

Materials

Chitosan (CTS) powder (with 85% deacetylation, mean molecular weight 250,000 Da) used in the present study was obtained from Marine Chemicals, Kochi (India). Itaconic acid (IA), ammonium per sulphate (APS), glutaraldehyde and acetone were purchased from S.d. Fine Chem, Bangalore (India). Cloisite 30B and acid modified multiwalled carbon nanotubes (MWCNT) were procured from Global Nanotech, Mumbai (India). Congo red (CR) was purchased from Himedia Laboratories, Mumbai (India). Silane treated nanoclay, naphthol green (NG) and reactive black (RB) were purchased from Sigma Aldrich, USA. All other solvents used were obtained from S.d. Fine Chemicals, Bangalore (India) and were used as received.

Synthesis of Chitosan grafted Itaconic acid (CTS-g-IA)

IA (3g) was dissolved in 100 ml distilled water in a 250 ml beaker equipped with a mechanical stirrer. 1g of CTS was then added to the dispersion and was kept stirring for few minutes till CTS was completely dissolved. 100 mg of APS initiator and 30% of glutaraldehyde as crosslinker was then added to the reaction mixture under continuous stirring. Further, the reaction mixture was then subjected to microwave irradiation using locally fabricated Microwave reactor (Enerzi Microwave Systems, India) at 60˚C for 10 minutes using a power of 800W. The reaction mixture of CTS-g-IA was cooled to room temperature and the mixture was neutralized using 1N sodium hydroxide (NaOH) till the pH reached 7. This was followed by precipitation using acetone. The precipitate obtained was washed several times with acetone and kept for drying at 50°C for 5-6 hours. The dried CTS-g-IA were then grounded into a fine powder and stored in a zip lock cover for further use.

For the synthesis of CTS-g-IA with nanoclay, cloisite 30B and acid modified MWCNT (separately), similar procedure was followed except that 5% nanoparticles were added for each case to the CTS and IA mixture and sonicated for about 30 minutes using Ultra Sonicator (Branson, 2510E/DTH) prior to microwave irradiation.

Fourier Transform Infrared (FTIR) Spectroscopy

The Fourier transform infrared spectroscopy (FTIR) analysis of Chitosan and CTS-g-IA nanocomposites were recorded between 600 and 4000 cm^{-1} using a FTIR spectrophotometer (Alpha-Bruker, 200621 ATR Model)

X-ray diffraction studies

X-ray diffraction (XRD) measurements for the adsorbent nanocomposites were performed using advanced diffractometer (PANalytical, XPERT-PRO) equipped with Cu-Kα radiation source (X = 0.154 nm). The diffraction data were collected in the range of $2\theta = 3 – 60^{\circ}$ with fixed time mode keeping the interval at 0.05°.

Scanning electron microscopy (SEM)

The morphological characterization for the nanocomposites was carried out using a scanning electron microscope (JEOL, JSM-840A). The specimens were gold sputtered before imaging as they are non-conducting.

Transmission electron microscopy (TEM)

Transmission electron microscopy (TEM) for nanocomposites was performed using a JEOL, Model 782, operating at 200 kV. TEM specimens were prepared by dispersing the composite powders in methanol by ultrasonication. A drop of the suspension was put on a TEM support grid (300 mesh copper grid coated with carbon). After drying in air, the composite powder remained attached to the grid and was viewed under the transmission electron microscope.

Water absorbency and swelling kinetics

Swelling behaviour of the adsorbent materials namely chitosan grafted itaconic acid (CTS-g-IA), chitosan grafted itaconic acid with nanoclay (CTS-g-IA/NC), chitosan grafted itaconic acid with multi-walled carbon nanotubes (CTS-g-IA/MWCNT) and chitosan grafted itaconic acid with cloisite 30B (CTS-g-IA/cloisite 30B) in various buffer mediums were measured as follows: 0.1 ± 0.02 g of samples were placed in 25 ml beakers into which 10 ml of buffer solutions with pH 7, pH 9 and pH 4 were then added separately. The weight of swollen sample was noted every 10 minutes till it reached equilibrium. The excess water on the surface was removed by gently tapping the swollen sample with a dry filter paper. Swelling (S) of sample was measured by weighing the swollen and the dry samples. Swelling (S) of sample was calculated using the equation given below.

$$\text{Swelling (S) in (g/g)} = \frac{(W_t - W_0)}{W_0} \quad (1a)$$

where, W_0 and W_t are the weights of the dry sample and the swollen sample at the time t, respectively.

The equilibrium swelling (E_S) of sample was calculated by using following equation:

$$\text{Equilibrium Swelling } (E_S) \text{ in } (g/g) = \frac{(W_e - W_0)}{W_0} \quad (1b)$$

Here W_e is the mass of the swollen sample at equilibrium.

Dye removal studies

Dye adsorption was carried out by immersing the 0.05 ± 0.01 g of CTS grafted IA into 20 ml of dye solution. All adsorption experiments were carried out by batch method. To study the adsorption kinetics, at specified time intervals, the amount of adsorbed congo red (CR), naphthol green (NG) and reactive black (RB) dyes were evaluated using a UV spectrometer at λ_{max} = 498, 714 and 596 nm, respectively. The dye removal percentage (R%) and the adsorption capacity or dye removal efficiency (q_t, mg/g) was calculated using following Equations given below. Similar procedure was carried out for the composite with optimal concentration of nanoclay, MWCNT and cloisite 30B. Standard solutions of congo red, naphthol green and reactive black dyes were prepared for five different concentrations namely 10 mg/L, 20 mg/L, 30 mg/L,40 mg/L and 50mg/L.

$$\text{Adsorption capacity, } q_t = \frac{(C_o - C_t)}{m} \times V \quad (2a)$$

$$\text{Dye removal percentage, } R\% = \frac{(C_o - C_e)}{C_0} \times 100 \quad (2b)$$

where, C_0 is the initial dye concentration (mg/L), C_t is the remaining dye concentrations in the solution at time t (mg/L), C_e is the remaining dye concentration in the solution at equilibrium (mg/L), V is the volume of dye solution used in litres (L) and m is the weight of adsorbent (mg).

Adsorption isotherm models

Different isotherm models were applied in order to analyse the characteristic parameters of the adsorption process like adsorption capacity and adsorbate concentration. In this study, three isotherm models namely Langmuir, Freundlich and Harkins-Jura were used to fit the experimental data.

Langmuir model assumes formation of monolayer adsorption on a homogenous adsorbent surface and no further adsorption occurs thereafter [**23**]. Langmuir isotherm can be represented as linear equation as follows:

$$\frac{C_e}{q_e} = \frac{1}{K_L * q_m} + \frac{C_e}{q_m} \quad (3)$$

where q_m is the maximum monolayer adsorption capacity (mg/g), K_L = Langmuir isotherm constant (L/mg), C_e = equilibrium concentration of adsorbate (mg/L) and q_e = amount of adsorbate per gram of adsorbent at equilibrium (mg/g). q_m and K_L values can be obtained from slope and intercept of linear plot of $1/q_e$ versus $1/C_e$.

Freundlich isotherm model is commonly used to describe adsorption characteristics for heterogenous surfaces [**24**]. This isotherm model can be represented as follows:

$$\ln q_e = \frac{1}{n_F} \ln C_e + \ln K_F \quad (4)$$

where K_F = Freundlich isotherm constant ($mg^{1-1/n}L^{1/n}g^{-1}$), $1/n_F$ = constant indicating adsorption intensity, C_e = equilibrium concentration of adsorbate (mg/L) and q_e = amount of adsorbate per gram of adsorbent at equilibrium (mg/g). The intercept K_F and the slope $1/n_F$ can be obtained by plotting $\ln q_e$ against $\ln C_e$.

Harkins-Jura (H-J) isotherms model assumes the possibility of multilayer adsorption on the surface of adsorbents having heterogeneous pore distribution [**25**]. This isotherm model can be represented as follows:

$$\frac{1}{q_e^2} = \frac{B}{A} - \frac{1}{A} \log C_e \quad (5)$$

where, A and B are H-J constants, C_e = equilibrium concentration of adsorbate (mg/L) and q_e = amount of adsorbate per gram of adsorbent at equilibrium (mg/g). Constants A and B can be obtained from plot $1/q_e^2$ versus $\log C_e$.

Results and discussion

FTIR analysis

FTIR spectrograms of pure CTS, IA and CTS-g-IA have been shown in **Fig. 1**. FTIR spectrum of pure CTS shows the characteristic peak at 3430 cm^{-1}which represents the stretching vibration of -O-H, while the 1652 cm^{-1} peak shows the characteristic amide I carbonyl stretching and the peak at 1425 cm^{-1} correspond to the -C-H symmetrical deformation. The peaks at 1070 and 2885 cm^{-1} are related to (C-O-C) stretching vibration and aliphatic -C-H stretching vibration respectively [**26**]. Similar peaks have been discussed in detail by Wang *et. al.* [**27**]. Pure itaconic acid shows peaks at 1705 cm^{-1} for C=O and 1630 cm^{-1} for C=C stretching vibrations. CTS grafted IA showed newer characteristic peaks at 1741, 1638 and 1562 cm^{-1} for C=O, C=N and $-NH_3^+$ respectively as similarly observed by Ge *et. al.* [**28**]. This indicates formation of the grafted product.

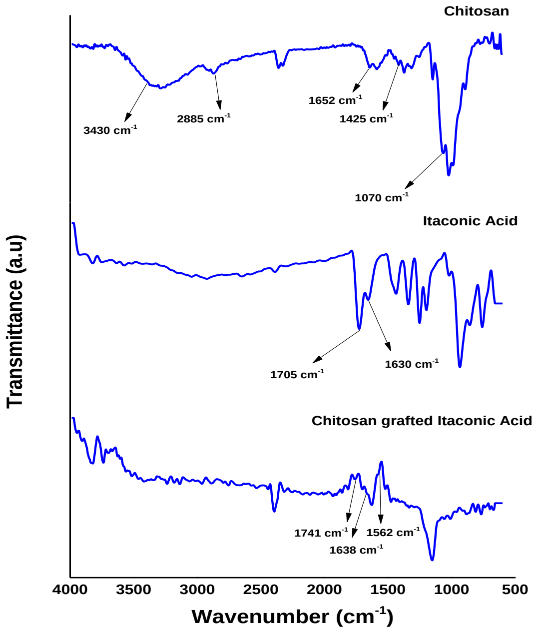

Fig. 1. FTIR spectra of CTS, IA and CTS-g-IA.

XRD analysis

XRD analysis has been studied in order to assess the dispersion of nanomaterials within the CTS-g-IA composites. XRD diffractograms for CTS-g-IA nanocomposites are shown in Figure 2-4. The XRD pattern of CTS-g-IA showed small peaks at 2θ values of 4.1^o, 10.7^o, 18.41^o and 34.19^o which indicate predominant amorphous nature of chitosan. In **Fig. 2**, the XRD pattern of nanoclay exhibit characteristic crystalline peaks at 2θ values of 7.8^o, 19.73^o, 24.17^o and 34.78^o. XRD of CTS-g-IA/NC shows similar peaks as of CTS-g-IA, however, the peaks at 2θ values of 7.8^o, 24.17^o and 34.78^o has been disappeared indicating nanoclay has been exfoliated in the composite. Similar observations on chitosan–nanoclay bionanocomposites have been made by Ghelejlu *et. al.* [**29**].

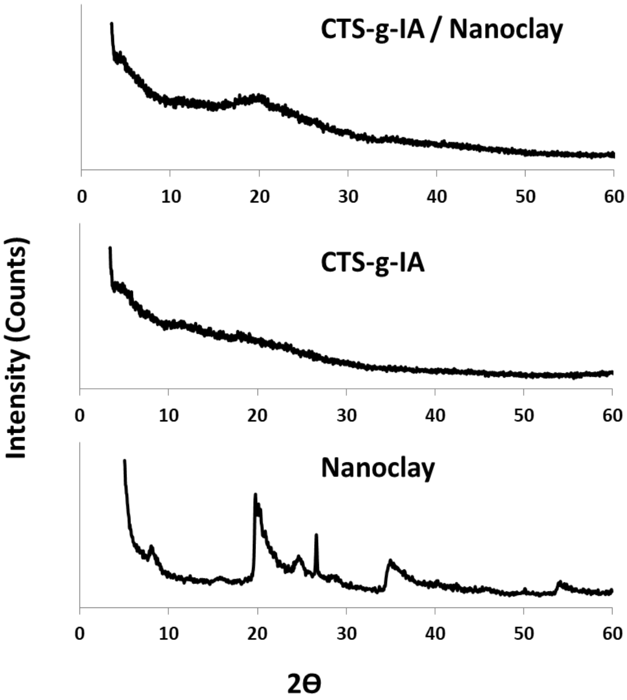

Fig. 2. X-ray diffractograms of CTS-g-IA nanocomposites and nanoclay.

Fig. 3 showed XRD diffractograms of CTS-g-IA/cloisite 30B. In case of cloisite 30B, the major crystalline peaks are observed at 2θ values of 3.85^o, 7.2^o, 20.03^o and 34.78^o. For the CTS-g-IA/cloisite 30B nanocomposites, it can be observed that the peaks at 2θ values of 3.85^o, 7.2^o and 34.78^o have been disappeared. This indicates that the crystalline structure of cloisite 30B has been destroyed in the nanocomposites. Hence, there exists a combination of intercalated-exfoliated structure owing to silicate interlayer interactions. Similar observations have been made by Wang *et. al.* for CMC/ organic montmorillonite nanocomposites [**30**].

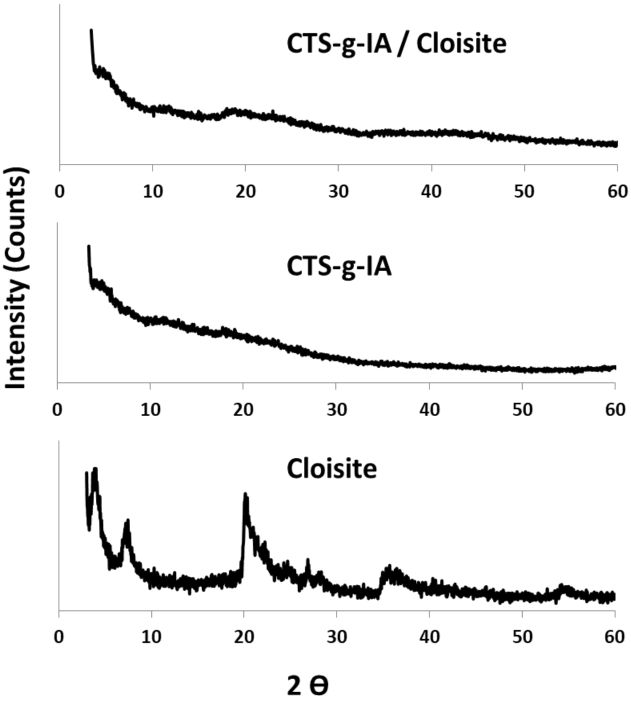

Fig. 3. X-ray diffractograms of CTS-g-IA nanocomposites and cloisite.

From **Fig. 4**, it can be observed that XRD pattern of MWCNT showed the typical peaks at 2θ values of 23.6^o and 43.5^o. However, the two peaks of MWCNT are absent in the XRD pattern of CTS-g-IA/MWCNT which indicates dispersion of MWCNTs within the CTS-g-IA composites [**31**].

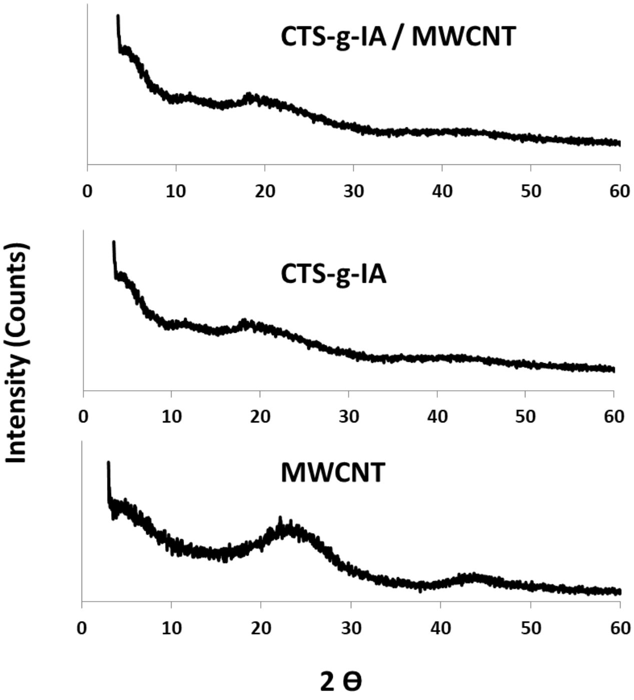

Fig. 4. X-ray diffractograms of CTS-g-IA nanocomposites and MWCNT.

Overall, it can be observed that all the three CTS-g-IA nanocomposites have been exhibited broad diffractograms which indicates predominately amorphous structure of the particles. The presence of amorphous structure in turn benefits the adsorption capacity of the nanocomposites as suggested by Luo *et. al.* [**32**] and Li *et. al.* [**33**].

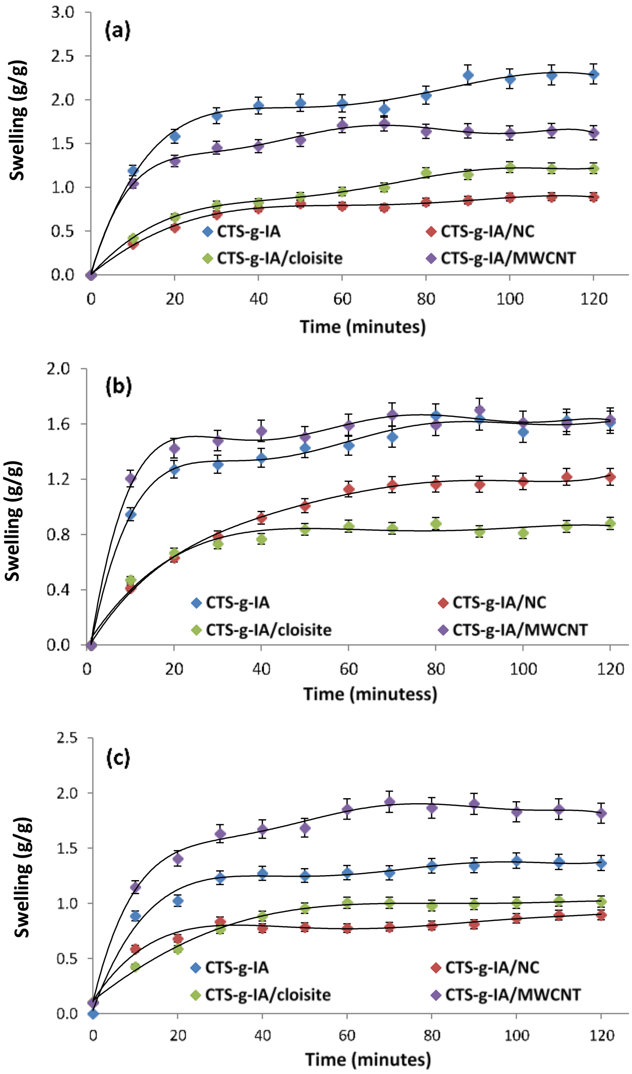

Fig. 5. Swelling characteristics of nanocomposites in (a) acidic (pH 4) medium, (b) neutral (pH 7) medium and (c) basic (pH 9) medium.

Swelling behaviour of nanocomposites in various buffer solutions

The swelling behaviour of CTS-g-IA nanocomposites in acidic, basic and neutral buffer solutions with time were investigated and results are shown in **Fig. 5(a-c)**. The Equilibrium swelling values and pseudo second order kinetic parameter of nanocomposites in various buffer mediums are listed in **Table 1**. From the figures, it can be observed that all the nanocomposites exhibits similar swelling pattern with time in the buffer solutions. All the nanocomposites showed higher rate of swelling till 60 min, beyond which equilibrium is reached with no further water uptake. Further, from **Table 1** it can be observed that incorporation of nanoparticles like cloisite 30B and nanoclay reduced the E_S values of nanocomposites in all the buffer solutions. This reduction in swelling might be due to the increased loading quantities (up to 5%), as nanoclays reduces the elasticity of the polymer chains leading to lowering of swelling rates [**34**]. According to studies on inorganic superabsorbent hydrogels by Zhang *et. al.* [**35**], presence of higher concentration of nano sized clays increases the crosslinking density between the polymer networks by filling the voids between them. Thus, reduces the swelling capacity of nanocomposites.

On the other hand, it can be observed that the swelling behaviour of CTS-g-IA nanocomposites with MWCNT is closer to that of CTS-g-IA in acidic (pH 4) and neutral (pH 7) medium. However, in basic (pH 9) medium, the CTS-g-IA/MWCNT have shown higher value of E_S than CTS-g-IA. This increase in the swelling capacity of MWCNT nanocomposites can be attributed to the hydrophilic nature of acid functionalized MWCNT in alkaline medium. Similar observations on functionalized MWCNT and PVA nanocomposites have been made by Jose *et. al.* [**36**], in which, it has been stated that the higher loading of acid functionalized CNT induces more hydrophilic nature to the polymer matrix in water-ethanol mixtures.

Table 1. Equilibrium swelling values and linearized pseudo-second order kinetic parameter of nanocomposites in various buffer medium.

Sample	**Buffers Solution pH4**				**Buffer Solution pH9**			
	Es	**Ei**	**Ki**	**$<R^2>$**	**Es**	**Ei**	**Ki**	**$<R^2>$**
CTS-g-IA	2.281	2.492	0.188	0.989	1.384	1.452	0.204	0.998
CTS-g-IA/ Nanoclay	0.883	0.971	0.162	0.994	0.892	0.924	0.119	0.991
CTS-g-IA/ Cloisite	1.224	1.431	0.061	0.985	1.021	1.163	0.078	0.993
CTS-g-IA/ MWCNT	1.632	1.732	0.325	0.995	1.834	1.961	0.314	0.996

Sample	**Buffers Solution pH7**			
	Es	**Ei**	**Ki**	**$<R^2>$**
CTS-g-IA	1.650	1.753	0.186	0.994
CTS-g-IA/ Nanoclay	1.184	1.372	0.060	0.995
CTS-g-IA/ Cloisite	0.881	1.091	0.077	0.980
CTS-g-IA/ MWCNT	1.611	1.692	0.438	0.997

Swelling kinetics

Linearized pseudo-second order swelling kinetic model has been used to evaluate the swelling kinetics of CTS-g-IA nanocomposites in acidic, alkaline and neutral medium. Linearized pseudo-second order swelling kinetic model can be represented as Equation 6 [**37**].

$$\frac{t}{E_t} = \frac{1}{K_i} + \left(\frac{1}{E_i}\right) t \tag{6}$$

where, E_t is the swelling (g/g) at a given time t (minutes), E_i is the theoretical equilibrium swelling (g/g), K_i is the initial swelling rate constant (g/g/min).

The t/E_t versus t plots for experimental swelling data showed straight lines with linear correlation coefficient $<R^2>$ value greater than 0.96, thus indicating suitability of this model for evaluating the kinetic swelling behavior of CTS-g-IA nanocomposites. By using equation 6, swelling kinetic parameters like swelling rate constant (K_i) and theoretical equilibrium adsorption (E_i) were calculated from the slope and intercept of the linear lines shown in **Fig. 6(a-c)**. These values are listed in Table 1. It can be observed that experimental results (E_S) matched closely with the theoretical results (E_i) from linearized pseudo-second order kinetic model.

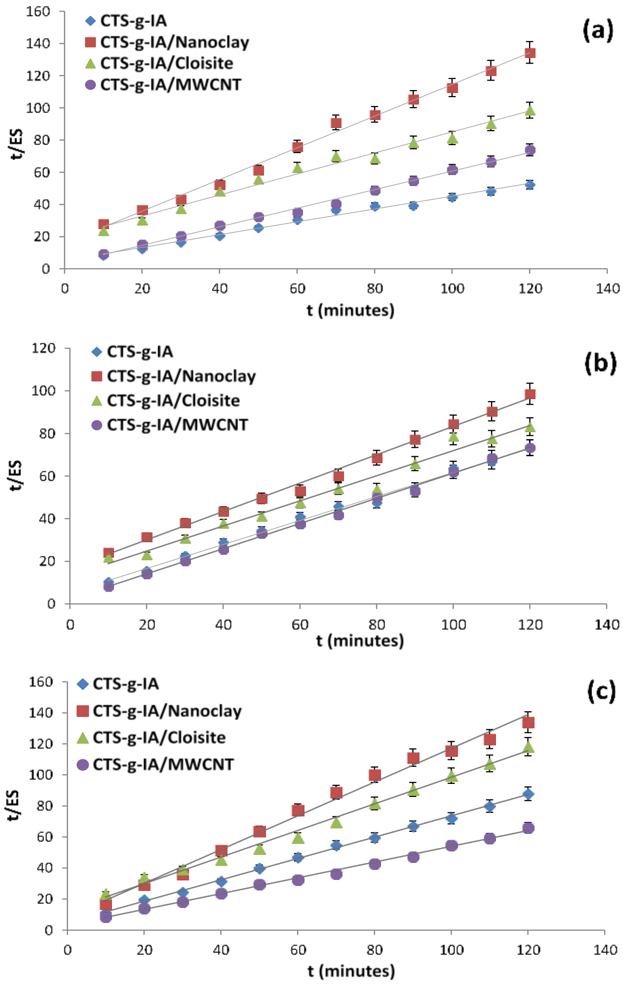

Fig. 6. Linearized form of pseudo-second order kinetic model for nanocomposites in (a) acidic (pH 4) medium, (b) neutral (pH 7) medium and (c) basic (pH 9) medium.

Dye removal studies

I. Congo red (CR) dye adsorption

The efficiency of adsorption of CR dye using CTS-g-IA nanocomposites by varying initial dye concentration has been shown in **Fig. 7**. From the figure it can be noted that the CR dye removal capacity of all nanocomposites increased with the increase in initial dye concentration. Many researchers have noted similar observations stating that the adsorbing capacity of the adsorbent is enhanced due to the increase in driving force of the dye concentration with higher initial concentration, which in turn helps in lowering the mass transfer resistance between the dye solution and the solid adsorbent [**38-42**].

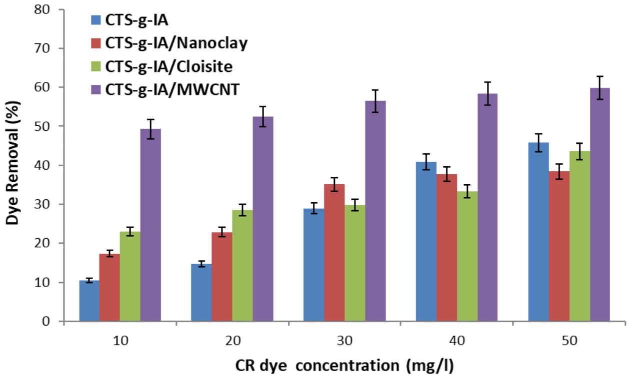

Fig. 7. Percentage of CR dye removal efficiency of nanocomposites with varying initial dye concentration.

Effects of nanoparticles on percentage removal of CR dye are also shown in **Fig. 7**. At lower initial dye concentration of 10, 20, 30 mg/L, addition of nanoclay and cloisite 30B loaded separately into the CTS-g-IA led to increased level of percentage removal of dye (i.e., from 10%, 17% and 23% respectively for 10 mg/L initial dye concentration). The percentage of dye removal were respectively 15%, 23% and 28% for 20mg/L initial dye concentration while 28%, 35% and 30% respectively for 30mg/L initial dye concentration. However, at higher initial concentration (40mg/L and 50mg/L initial dye concentration) slight decrease in percentage dye removal has been observed. This might be due to the saturation of adsorption sites in the nanocomposites. Similar observations have been made by Feng *et. al.* [**43**]. Further it can be observed that CTS-g-IA/MWCNT nano-composites showed better adsorption levels as compared to cloisite 30B and nanoclay based nanocomposites. Higher initial dye concentration enhanced the percentage of dye removal from 49% to 60% for 10 mg/L and 50mg/L dye concentrations, respectively. This higher dye removal efficiency is attributed to the porous surface area and presence of hydroxyl and carboxyl groups on the MWCNT surface owing to acid modification of MWCNT [**44**]. Similar observation of better removal of CR dye using MWCNT composites have been made by Chatterjee *et. al.* [**45**] and Shirgholami *et. al.* [**46**].

Adsorption isotherm models were fitted for CR dye removal results with different initial dye concentrations. **Fig. 8(a-c)**, shows Langmuir, Freundlich and Harkins-Jura isotherms for CR dye adsorption on CTS-g-IA nanocomposites. Isotherm parameters for Langmuir, Freundlich and Harkins-Jura models along with their respective correlation coefficients <R^2> values have been given in **Table 2(a)**. It can be observed that, Langmuir model showed better dye removal efficiency with <R^2> values more than 0.99. Thus, this indicated that Langmuir isotherm show a good fit to the experimental data than Freundlich and Harkins-Jura isotherms for CR dye adsorption. From **Table 2(a)**, it can also be observed that the adsorption capacity (q_m) value is higher for MWCNT nanocomposites (232.554 mg/g) as compared to nanoclay (151.512 mg/g) and cloisite 30B nanocomposites

(166.663 mg/g). This is in agreement with the enhanced percentage of CR dye removal by CTS-g-IA/MWCNT nanocomposites than nanoclay and cloisite 30B nanocomposites as observed in Figure 3(a). From values of 'q_m' it can be noted that the CR dye adsorption capability of the nanocomposites were in the order CTS-g-IA/MWCNT > CTS-g-IA/C\cloisite 30B > CTS-g-IA/nanoclay > CTS-g-IA.

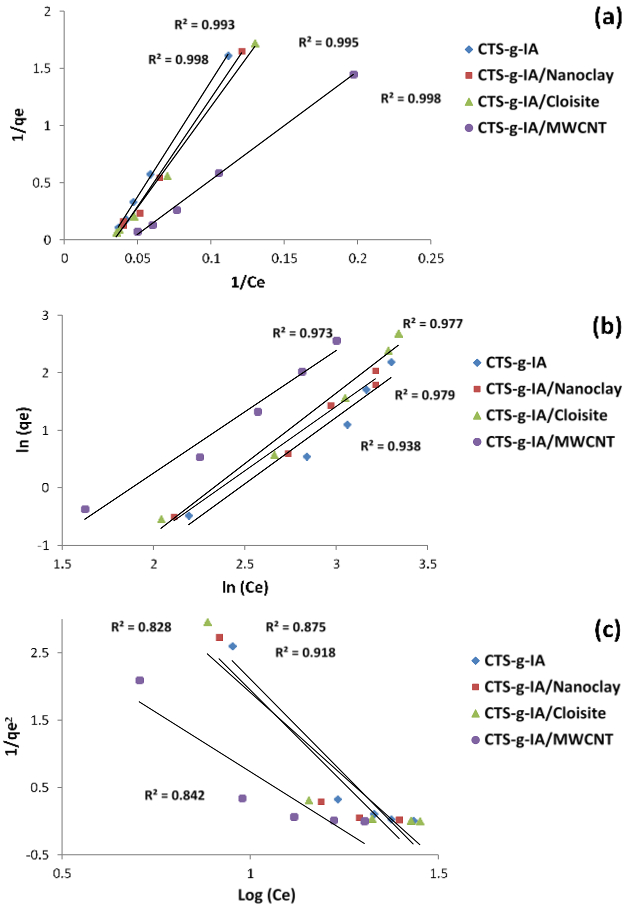

Fig. 8. (a) Langmuir isotherms; (b) Freundlich isotherms and (c) Harkins-Jura isotherms for CR dye adsorption on nanocomposites.

Table 2(a). Langmuir, Freundlich and Harkins-Jura isotherms parameters for CR dye adsorption onto CTS-g-IA nanocomposites.

Sample	Langmuir Isotherm			Freundlich Isotherm			Harkins-Jura Isotherm		
	q_m (mg/g)	K_L (L/mg)	<R²>	$1/n_F$	K_F ($mg^{1-1/n}$ $L^{1/n}$ g^{-1})	<R²>	A (mg/g)	B	<R²>
CTS-g-IA	158.731	0.031	0.998	0.560	8.782	0.938	0.145	1.133	0.918
CTS-g-IA/ Nanocaly	151.512	0.035	0.993	0.612	7.984	0.979	0.237	1.253	0.875
CTS-g-IA/ Cloisite	166.663	0.037	0.995	0.641	8.971	0.977	0.476	1.571	0.828
CTS-g-IA/ MWCNT	232.554	0.045	0.998	0.753	14.524	0.973	1.073	1.933	0.842

II. Naphthol green (NG) dye adsorption

The adsorption studies of CTS-g-IA nanocomposites were carried out with varying initial concentration of NG dye. **Fig. 9** showed the effect on dye removal efficiency with varying initial dye concentration. It can be observed that percentage removal of NG dye by all the nanocomposites gradually increased by increasing the initial concentration. However, CTS-g-IA composite with cloisite 30B exhibited highest adsorption rate when compared to others. It has been noted that the dye removal percentage was increased from 11% for 10mg/L to 40% for 50mg/L initial concentration. This might be due to the presence of hydroxyl groups on the cloisite 30B which makes it more efficient for the removal of acidic dyes [**39-41,47**]. Similar observations have been made by Vanaamudan *et. al.* where nanocomposites comprised of chitosan and cloisite 30B have been found to be favourable for reactive blue and reactive red [**48**].

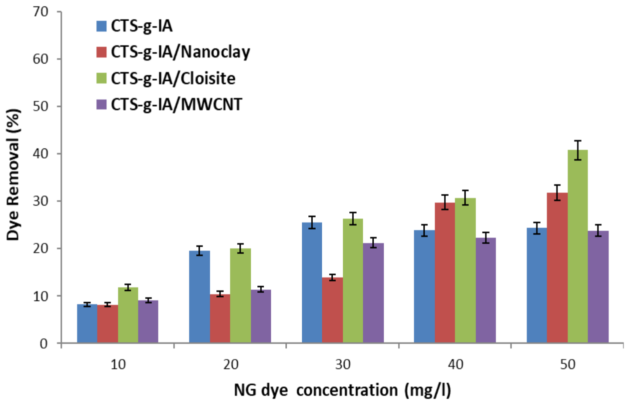

Fig. 9. Percentage of NG dye removal efficiency of nanocomposites with varying initial dye concentration.

Fig. 10(a-c), shows adsorption isotherm models for NG dye adsorption on CTS-g-IA nanocomposites. Isotherm parameters for Langmuir, Freundlich and Harkins-Jura models and their respective correlation coefficients <R²> values are presented in **Table 2(b)**. It can be observed that, Langmuir model showed better adsorption results with <R²> values more than 0.98. Thus, this indicates that Langmuir isotherm showed a good fit to experimental data than Freundlich and Harkins-Jura isotherms for NG dye removal. It can also be observed that the adsorption capacity (q_m) value is higher for cloisite 30B nanocomposites (158.731 mg/g) as compared to nanoclay (135.133 mg/g) and MWCNT nanocomposites (149.252 mg/g) shown in Figure 9.

Table 2(b). Langmuir, Freundlich and Harkins-Jura isotherms parameters for NG dye adsorption onto CTS-g-IA nanocomposites.

Sample	Langmuir Isotherm			Freundlich Isotherm			Harkins-Jura Isotherm		
	q_m (mg/g)	K_L (L/mg)	<R²>	$1/n_F$	K_F ($mg^{1-1/n}$ $L^{1/n}$ g^{-1})	<R²>	A (mg/g)	B	<R²>
CTS-g-IA	142.850	0.025	0.994	0.531	9.162	0.987	0.107	1.124	0.799
CTS-g-IA/ Nanocaly	135.133	0.031	0.995	0.444	8.181	0.922	0.119	1.081	0.897
CTS-g-IA/ Cloisite	158.731	0.030	0.993	0.425	8.021	0.978	0.113	1.190	0.841
CTS-g-IA/ MWCNT	149.252	0.035	0.992	0.532	8.543	0.986	0.121	1.151	0.825

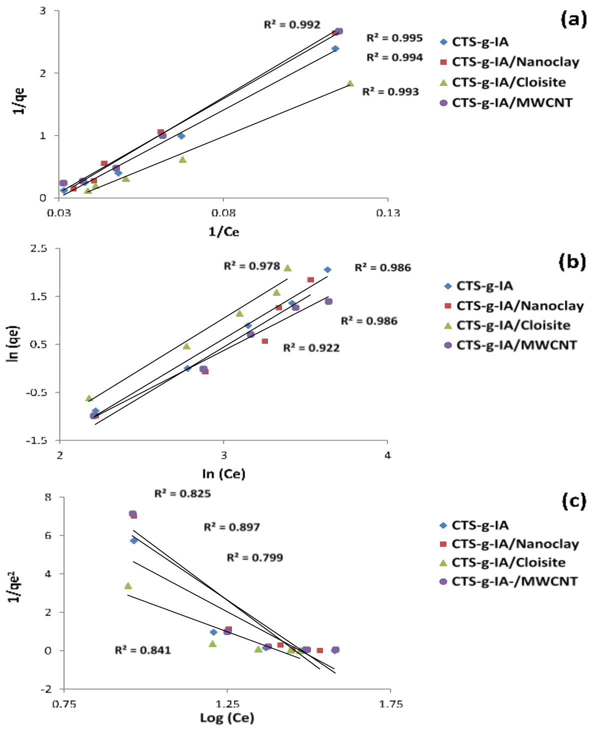

Fig. 10. (a) Langmuir isotherms; (b) Freundlich isotherms and (c) Harkins-Jura isotherms for NG dye adsorption on nanocomposites.

III. Reactive black (RB) dye adsorption

The effects of initial RB dye concentration on the adsorption of CTS-g-IA nanocomposites are shown in **Fig. 11**. It has been observed that the percentage removal of RB dye gradually increased with the increasing initial concentration for all the nanocomposites. Further, it is also observed that CTS-g-IA/MWCNT nanocomposite exhibited better dye removal percentage as compared to cloisite 30B and nanoclay nanocomposites. Increase in initial dye concentration from 10 mg/L to 50mg/L, increased the percentage dye removal from 36% to 56%, respectively. This higher adsorption capacity is attributed to the porous surface area and presence of hydroxyl and carboxyl groups on the MWCNT surface owing to acid modification of MWCNT [**39-41,43**]. Similar work has been carried out by Bazrafshan *et. al.* where it is observed that the MWCNTs were able to remove up to 98% of dye from reactive black 5 solution [**49**].

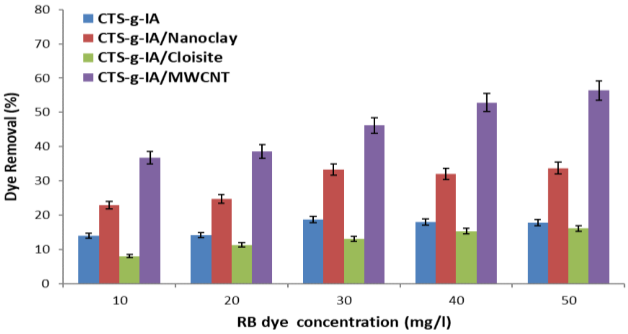

Fig. 11. Percentage of RB dye removal efficiency of nanocomposites with varying initial dye concentration.

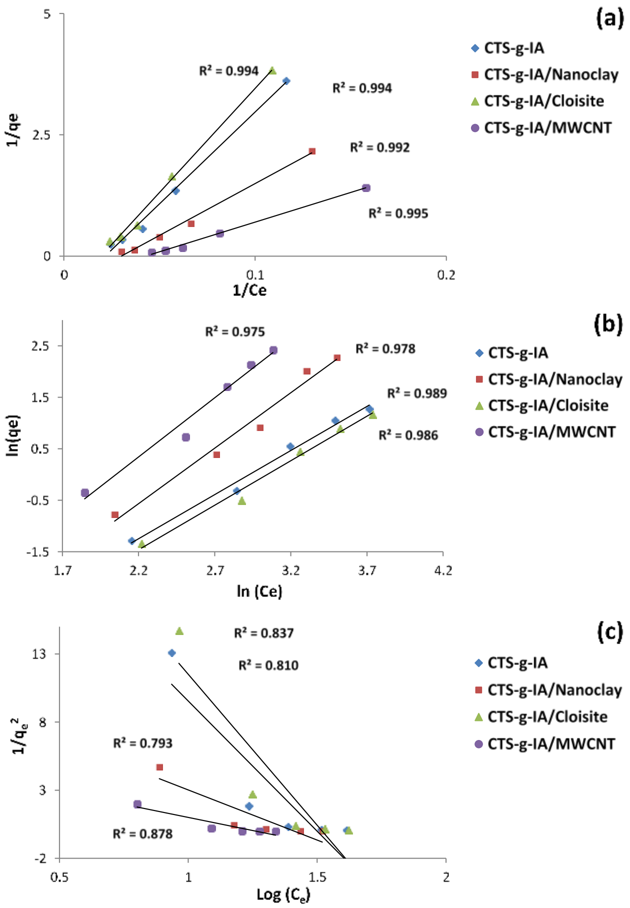

Fig. 12. (a) Langmuir isotherms; (b) Freundlich isotherms and (c) Harkins-Jura isotherms for RB dye adsorption on nanocomposites

Adsorption isotherm models have been fitted for dye adsorption results with different initial RB dye concentration. **Fig. 12(a-c)**, shows Langmuir, Freundlich and Harkins-Jura isotherms for RB dye adsorption on CTS-g-IA nanocomposites. Isotherm parameters along with their respective correlation coefficients <R^2> values are given in **Table 2(c)**. It can be observed that, Langmuir model illustrate a good fit to the experimental data than Freundlich and Harkins-Jura isotherms for RB dye adsorption. Correlation coefficients <R^2> values for the nanocomposites were found to be more than 0.99.

Table 2(c). Langmuir, Freundlich and Harkins-Jura isotherms parameters for RB dye adsorption onto CTS-g-IA nanocomposites.

Sample	Langmuir Isotherm			Freundlich Isotherm			Harkins-Jura Isotherm		
	q_m (mg/g)	K_L (L/mg)	<R^2>	$1/n_F$	K_F ($mg^{1-1/n}$ $L^{1/n}$ g^{-1})	<R^2>	A (mg/g)	B	<R^2>
CTS-g-IA	123.453	0.021	0.994	0.307	7.030	0.985	0.587	1.344	0.810
CTS-g-IA/ Nanocaly	156.254	0.029	0.992	0.413	8.512	0.978	0.336	1.432	0.793
CTS-g-IA/ Cloisite	119.042	0.020	0.994	0.654	7.190	0.986	0.269	1.511	0.837
CTS-g-IA/ MWCNT	192.301	0.045	0.995	0.608	11.623	0.964	1.007	1.281	0.878

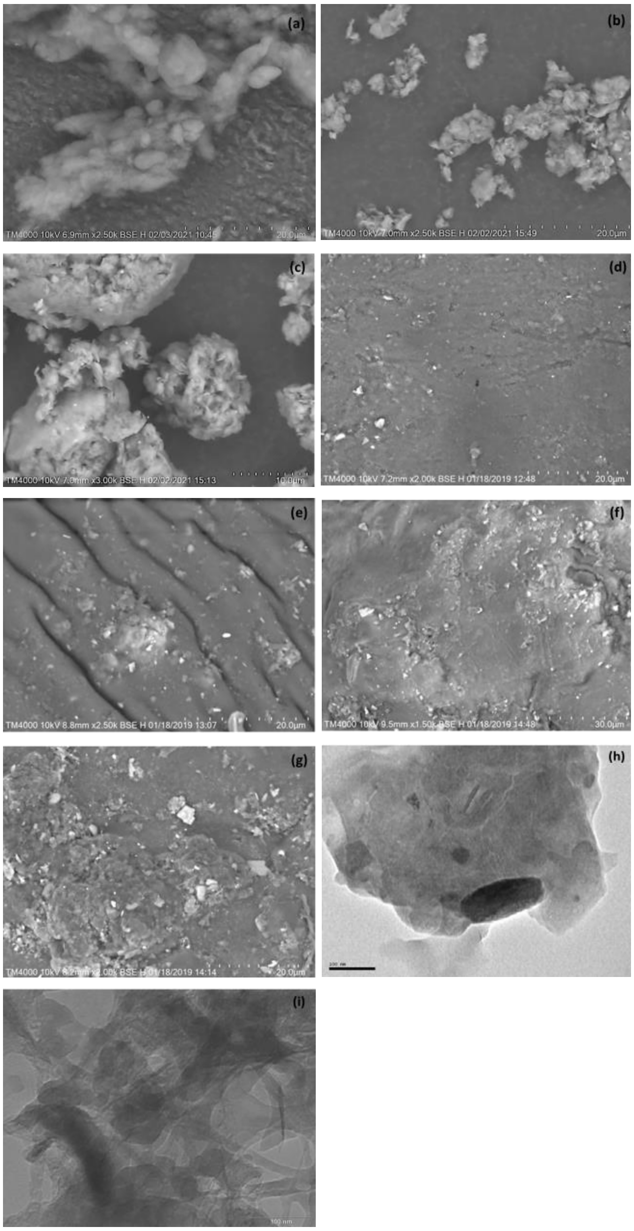

Fig. 13. (a) SEM micrograph of pure MWCNT. (b) SEM micrograph of pure nanoclay. (c) SEM micrograph of pure cloisite 30B. (d) SEM micrograph of CTS-g-IA composites. (e) SEM micrograph of CTS-g-IA /Nanoclay nanocomposites. (f) SEM micrograph of CTS-g-IA/Cloisite nanocomposites. (g) SEM micrograph of CTS-g-IA/MWCNT nanocomposites. (h) TEM micrograph of CTS-g-IA/MWCNT nanocomposites. (i) TEM micrograph of CTS-g-IA/Nanoclay nanocomposites.

Morphology

The SEM micrographs of nanocomposites along with pure nanomaterials are shown in **Fig. 13(a-g)**. SEM micrograph of pure MWCNT (**Fig. 13(a)**) showed tube like structure intermingled with each other. On the other hand both nanoclay (**Fig. 13(b)**) and cloisite 30B (**Fig. 13(c)**) showed needle like structure fused with one another formed bulging. **Fig. 13(d)** showed the SEM micrograph of grafted chitosan, is predominantly a smooth surface. Grafted chitosan loaded with nanoclay shows a rugged layered surface (**Fig. 13(e)**) while chitosan loaded with cloisite shows a relatively smoother morphology as shown in **Fig. 13(f)**. However grafted chitosan loaded with MWCNT shows predominantly rough surface morphology (**Fig. 13(g)**). TEM micrographs of the nanocomposites are depicted in Fig. **13(h-i)**. The TEM micrograph for grafted chitosan with MWCNT showed both dispersed and agglomerated domains (**Fig. 13(h)**). A similar observation can be made for nanoclay loaded grafted chitosan shown in **Fig. 13(i)**. The rough and rugged surface helps enhance the availability of specific surface area which in turn leads to enhanced adsorption capacities for trapping of dyes [**50, 51**]. Further, it can also be observed that dye adsorbability was relatively higher in MWCNT and nanoclay loaded grafted chitosan as compared to that with cloisite 30B (which has a smooth surface morphology, similar to neat grafted chitosan).

Conclusion

Chitosan has been grafted with itaconic acid along with nanoclay, cloisite 30B and MWCNT separately via microwave assisted reaction. Removal of napthol green, reactive black and congo red dyes were studied for all the three nano composites. The presence of rigid nanosized materials slightly reduced the equilibrium swelling capabilities. Congo red dye could be removed efficiently with MWCNT loaded grafted chitosan. Napthol green dye showed higher removal efficiency with closite 30 B loaded chitosan. MWCNT loaded grafted chitosan showed higher dye removal efficiency than the other two. XRD diffraction studies revealed the amorphous nature of the composites while morphological studies showed the rough surface morphology for the nanocomposites. Overall, these nanocomposites showed promising potential for the removal of toxic dye contaminants.

Conflicts of interest

There are no conflicts to declare.

Keywords

Chitosan, adsorption isotherm, nanoclay, MWCNT, dye removal.

Received: 9 November 2020
Revised: 5 February 2021
Accepted: 13 February 2021

References

1. Oliveira, E.H.C.; Fraga, D.M.S.M.; Silva, M.P.; Fraga, T.J.M.; Carvalho, M.N.; Freire, E.M.P.L.; Ghislandi, M.S.; Sobrinho, M.A.M.; *J. Environ. Chem. Eng*., **2019**, *7*, 1.
2. Yagub, M.T.; Sen, T.K.; Afroze, S.; Ang, H.M.; *Adv. Colloid Interface Sci*., **2014**, *209*, 172.
3. Reddy, N.S.; Krishna Rao, K.S.V.; *Indian. J. Adv. Chem. Sci*., **2016**, *4*, 214.
4. Sanghi, S.; Verma, P.; *Color. Technol*., **2013**, *129*, 85.
5. Szymczyk, P.; Filipkowska, U.; Jozwiak1, T.; Kuczajowska-Zadrożna, M.; *Prog. Chem. Appl. Chitin Derivatives*, **2015**, *20*, 206.
6. Ignat, M.; Dulman, V.; Onofrei, T.; *Cellulose Chem. Technol*., **2012**, *46*, 357.

7. Vakili, M.; Rafatullah, M.; Salamatinia, B.; Abdullah, A. Z.; Ibrahim, M. H.; Tan, K. B.; Gholami, Z.; Amouzgar, P.; *Carbohyd. Polym.*, **2014**, *113*, 115.
8. Xing, Y.; Sun, X.; Li, B.; *Polym. Eng. Sci*., **2009**, *49*, 272.
9. Sadeghi-Kiakhani, M.; Arami, M.; Gharanjig, K.; *J. Appl. Polym. Sci*., **2013**, *127*, 2607.
10. Perju, M. M.; Dragan, E. S.; *Ion Exch. Lett*., **2010**, *3*, 7.
11. Razmi, F. A.; Ngadi, N.; Rahman, R. A.; Kamaruddin, M. J.; *Chem. Eng. Trans*., **2017**, *56*, 121.
12. Jabli, M.; Baouab, M. H. V.; Roudesli, M. S.; Bartegi, A.; *J. Eng. Fiber Fabr*., **2011**, *6*, 1.
13. Yuan, B.; Qiu, L. G.; Su, H. Z.; Cao, C. L.; Jiang, J. H.; *Int. J. Biol. Macromol*., **2016**, *82*, 355.
14. Esquerdo, V. M.; Quintana, T. M.; Dotto, G. L.; Pinto, L. A.; *React. Kinet. Mech. Cat.*, **2015**, *116*, 105.
15. Yu, Z.; Dang, Q.; Liu, C.; Cha, D.; Zhang, H.; Zhu, W.; Zhang, Q.; Fan, B.; *Carbohyd. Polym*., **2017**, *172*, 28.
16. Silva, J. M.; Farias, B. S.; Gründmann, D. D. R.; Cadaval Jr, T. R. S.; Moura, J. M.; Dotto, G. L.; Pinto, L. A. A.; *J. Appl. Polym. Sci*., **2017**, *134*, 1.
17. Wang, L.; Wang, A.; *J. Chem. Technol. Biotechnol*., **2007**, *82*, 711.
18. Kaemkit, C.; Monvisade, P.; Siriphannon, P.; Nukeaw, J.; *J. Appl. Polym. Sci*., **2013**, *128*, 879.
19. Vanaamudan, A.; Sudhakar, P. P.; *J. Taiwan Inst. Chem. Eng*., **2015**, *55*, 145.
20. Wang, L.; Wang, A.; *J. Hazard. Mater.*, **2007**, *147*, 979.
21. Kheirandish, S.; Ghaedi, M.; Dashtian, K.; Heidari, F.; Pourebrahim, F.; Wang, S.; *Int. J. Biol. Macromol*., **2017**, *102*, 181.
22. Ozkahraman, B.; Bal, A.; Acar, I.; Guclu, G.; *Clean (Weinh)*, **2011**, *39*, 1001.
23. Langmuir, I.; *J. Am. Chem. Soc.*, **1918**, *40*, 1361.
24. Freundlich, H.; *Trans. Faraday Soc*., **1932**, *28*, 195.
25. Amin, M.T.; Alazba, A.A.; Shafiq, M.; *Sustainability*, **2015**, *7*, 15302.
26. Roy, P.; Sailaja, R.R.N.; *Int. J. Biol. Macromol*., **2015**, *73*, 170.
27. Wang, Y.; Dang, Q.; Liu, C.; Yu, D.; Pu, X.; Wang, Q.; Gao, H.; Zhang, B.; Cha, D.; *ACS Appl. Mater. Interfaces*, **2018**, *10*, 40302.
28. Ge, H.; Hua, T.; Wang, J.; *Int. J. Biol. Macromol*., **2017**, *95*, 954.
29. Ghelejlu, S. B.; Esmaiili, M.; Almasi, H.; *Int. J. Biol. Macromol*., **2016**, *86*, 613.
30. Wang, M.; Wang, L.; *Water. Sci. Eng*., **2013**, *6*, 272.
31. Deepthi, M. V.; Sailaja, R. R. N.; Ananthapadmanabha, G. S.; Avadhani, G. S.; *Polym. Plast. Technol. Eng*., **2014**, *53*, 1476.
32. Luo, J. Y.; Lin, Y. R.; Liang, B. W.; Li, Y. D.; Mo, X. W.; Zeng, Q. G.; *RSC Adv*., **2015**, *5*, 100898.
33. Li, L. H.; Xiao, J.; Liu, P.; Yang, W.; *Sci. Rep*., **2015**, *5*, 1.
34. Prasanna, K.; Deepthi, M. V.; Ashamol, A.; Sailaja, R. R. N.; *Polym. Plast. Technol. Eng.*, **2013**, *52*, 352.
35. Zhang, S.; Guan, Y.; Fu, G.Q.; Chen, B.Y.; Peng, F.; Yao, C.L.; Sun, R.C.; *J. Nanomater.*, **2014**, *2014*, 1.
36. Jose, T.; George, S. C.; Maya, M. G.; Thomas, S.; *J. Chem. Eng. Process. Technol*., **2015**, *6*, 1.
37. Ho, Y.S.; McKay, G.; *Process Biochem*., **1999**, *34*, 451.
38. Aljebori, A. M. K.; Alshirifi, A. N.; *Asian J. Chem*., **2012**, *24*, 813.
39. Mezenner, N. Y.; Bensmaili, A.; *Chem. Eng. J*., **2009**, *147*, 87.
40. Banerjee, S.; Chattopadhyaya, M.C.; *Arab. J. Chem*., **2013**, *10*, 1629.
41. Pathania, D.; Sharma, S.; Singh, P.; *Arab. J. Chem*., **2017**, *10*, 1445.
42. Sartape, A.S.; Mandhare, A.M.; Jadhav, V.V.; Raut, P.D.; Anuse, M.A.; Kolekar, S.S.; *Arab. J. Chem.*, **2017**, *10*, 3229.
43. Feng, T.; Zhang, F.; Wang, J.; Wang, L.; *J. Appl. Polym. Sci*., **2012**, *125*, 1766.
44. Zare, K.; Gupta, V. K.; Moradi, O.; Makhlouf, A. S. H.; Sillanpaa, M.; Nadagouda, M. N.; Sadegh, H.; Shahryari-Ghoshekandi, R.; Pal, A.; Wang, Z.; Tyagi, I.; Kazemi, M.; *J. Nanostruct. Chem*., **2015**, *5*, 227.
45. Chatterjee, S.; Lee, M. W.; Woo, S. H.; *Bioresour. Technol*., **2010**, *101*, 1800.
46. Shirgholami, M. A.; Mirjalili, M.; Nasirizadeh, N.; *Orient. J. Chem*., **2017**, *33*, 676.
47. Daraei, P.; Madaeni, S. S.; Salehi, E.; Ghaemi, N.; Ghari, H.S.; Khadivi, M.A.; Rostami, E.; *J. Membr. Sci*., **2013**, *436*, 97.
48. Vanaamudan, A.; Sudhakar, P. P.; *J. Taiwan. Inst. Chem. E*., **2015**, *55*, 145.
49. Bazrafshan, E.; Mostafapour, F. K.; Rahdar, S.; Mahvi, A. H.; *Desalination and Water Treatment*, **2015**, *54*, 2241.
50. Ferrer, A.; Quintana, E.; Filpponen, I.; Solala, I.; Vidal, T.; Rodríguez, A.; Laine, J.; Rojas, J.O.; *Cellulose*, **2012**, *19*, 2179.
51. Ahmed, S.; Pasquier, A.D.; Asefa, T.; Birnie, P.D.; *Adv. Eng. Mater*., **2011**, *1*, 879.